Real-time phase-front detector for heterodyne interferometers

Felipe Guzmán Cervantes,[1,*] Gerhard Heinzel,[1] Antonio F. García Marín,[1] Vinzenz Wand,[1] Frank Steier,[1] Oliver Jennrich,[2] and Karsten Danzmann[1]

[1]Max-Planck-Institut für Gravitationsphysik, Albert-Einstein-Institut Hannover, and Institut für Gravitationsphysik, Leibniz Universität Hannover, Callinstrasse 38, 30167 Hannover, Germany
[2]European Space Agency, European Space Research and Technology Centre, Keplerlaan 1, Postbus 299, 2200 AG Noordwijk, The Netherlands

*Corresponding author: felipe.guzman@aei.mpg.de

Received 11 December 2006; revised 16 April 2007; accepted 20 April 2007; posted 24 April 2007 (Doc. ID 77947); published 6 July 2007

We present a real-time differential phase-front detector sensitive to better than 3 mrad rms, which corresponds to a precision of approximately 500 pm. This detector performs a spatially resolving measurement of the phase front of a heterodyne interferometer, with heterodyne frequencies up to approximately 10 kHz. This instrument was developed as part of the research for the Laser Interferometer Space Antenna Technology Package interferometer and will assist in the manufacture of its flight model. Because of the advantages this instrument offers, it also has general applications in optical metrology. © 2007 Optical Society of America

OCIS codes: 040.2840, 010.7350, 120.2650, 120.3180, 120.5050, 140.3300.

1. Introduction

Many applications in optical metrology require precision measurements and characterization of laser beam wavefronts, as well as an accurate mode matching of laser beams. To this end, it is usual to perform various adjustments that are both complex and time consuming, based on repeated measurements of beam parameters [1]. Alternative methods are Shack–Hartmann sensors, which measure the shape of a single wavefront with an accuracy of typically $\lambda/100$ [2], and phase-shifting interferometry (PSI) [3,4], which typically reaches $\lambda/1000$ [5].

Similar to PSI, the relative phase is found by a mathematical algorithm [6,7] that is applied on the intensities sampled for $n \geq 4$ instantaneous operating points with equidistant phase increments. This happens in parallel at each pixel of the spatially resolving photodetector (CCD camera). The advantage of our method over conventional PSI is that the phase shift, normally implemented by a piezoelectric transducer (PZT), is intrinsically contained in the time-dependent sinusoid obtained from the interference of two electric fields at different frequencies (optical heterodyning). Thus, nonlinearities of PZT elements and additional electronics required to keep the interferometer at a specific operation point can be avoided [8].

This article describes an apparatus able to measure in real time the relative spatial structure between two interfering wavefronts in a heterodyne interferometer. This allows a quick and precise characterization of the mode mismatch between two beams in real time, making possible an online adjustment of the optical components according to the mode mismatch displayed. By using beams with known shape, this method can also be used to analyze surfaces and optical components (in transmission and reflection), reaching a sensitivity better than $\lambda/2000$, which corresponds in our case to a precision of approximately 500 pm at $\lambda = 1064$ nm (Nd:YAG laser).

Optical heterodyne interferometry [9,10] is a useful technique for measuring distance variations with subwavelength precision and large dynamic range. This concept is applied, for example, in the Laser Interferometer Space Antenna (LISA) Technology

0003-6935/07/214541-08$15.00/0

Package (LTP) [11], which utilizes a set of heterodyne Mach–Zehnder interferometers to measure relative changes in the separation of two drag-free test masses with a noise level better than 10 pm/$\sqrt{\text{Hz}}$ in the frequency range of 3–30 mHz. It is well known that heterodyne interferometers are susceptible to various noise sources [12,13] that corrupt the phase measurement. One important noise source is the wavefront imperfections of the interfering beams in combination with beam jitter [14,15]. This effect is of particular importance if quadrant photodiodes are used, which are often employed to obtain alignment signals from the interferometer. The error term induced by the spatial inhomogeneity of the wavefronts can be minimized if the interfering beams have identical shape. The device we present here allows one to match the shape of the wavefronts with a simple procedure, permitting an online adjustment of the optical components.

2. Theoretical Background

A. Interference Pattern and Heterodyne Interferometry

The electric field $\mathbf{E}_j(\mathbf{r}, t)$ of a linearly polarized light beam can be described as

$$\mathbf{E}_j(\mathbf{r}, t) = E_j \mathbf{p}_j \exp\{i[2\pi f_j t + \varphi_j + \psi_j(\mathbf{r})]\}, \quad (1)$$

where j is an index to distinguish several beams, the vector $\mathbf{p}_j$ describes the polarization, E_j is the amplitude of the electric field, and $\psi_j(\mathbf{r})$ is the spatial distribution of the phase front. The intensity distribution $I(\mathbf{r}, t)$ oscillates at the heterodyne frequency $f_{\text{het}} = f_2 - f_1$ and is proportional to $|\mathbf{E}_{\text{total}}(\mathbf{r}, t)|^2$, where $\mathbf{E}_{\text{total}}(\mathbf{r}, t) = \mathbf{E}_1(\mathbf{r}, t) + \mathbf{E}_2(\mathbf{r}, t)$ is the interference pattern. Assuming identical polarization vectors $\mathbf{p}_1 = \mathbf{p}_2$ and also that the differential coherence length of the laser used is much larger than the distance from the source to the recombination point of the interferometer, the heterodyne component can be described as

$$I(\mathbf{r}, t) = A(\mathbf{r})\{1 + C(\mathbf{r})\cos[2\pi f_{\text{het}} t - \varphi(\mathbf{r})]\}, \quad (2)$$

where $A(\mathbf{r})$ is a space-dependent factor, $C(\mathbf{r})$ describes the contrast in terms of the space $\mathbf{r}$, and

$$\varphi(\mathbf{r}) = [\varphi_1 + \psi_1(\mathbf{r})] - [\varphi_2 + \psi_2(\mathbf{r})] \quad (3)$$

gives the spatial dependence of the phase, where $\psi(\mathbf{r}) = \psi_1(\mathbf{r}) - \psi_2(\mathbf{r})$ is the spatial distortion of the phase distribution. Ideally, for identically shaped wavefronts $[\psi_1(\mathbf{r}) = \psi_2(\mathbf{r})]$, the longitudinal phase term $\varphi_1 - \varphi_2$, which is the usual interferometric quantity to be measured, contains the length measurement describing the path-length difference ΔL between the arms of the interferometer:

$$\Delta L = \frac{\lambda}{2\pi}(\varphi_1 - \varphi_2), \quad (4)$$

where $\lambda = c/f$ is the wavelength of the light. This path-length difference can be strongly influenced by environmental changes that usually (as in the LTP) disturb the main length measurement.

To maximize the contrast of the interferometer, the beams need to be matched. It is therefore useful to characterize the mismatch between them and to be able to optimize it in real time.

B. Spatially Resolved Phase Measurement

The relative geometry of two interfering beams can be described by the spatial structure of the functions $A(\mathbf{r})$, $C(\mathbf{r})$, and $\psi(\mathbf{r})$. The apparatus described here measures these three functions in the real-time interference pattern using a CCD camera and pixelwise data processing. To obtain the phase of a sinusoidal function as in Eq. (2), several mathematical approaches [6] can be used that are based on measuring n equidistant intensity samples $I_k = I(t_k)$, with $t_k = k\Delta t$, where k is an integer. The approach chosen for this experiment is a four-point algorithm [16], corresponding to a straightforward discrete Fourier transform of the signal with $n = 4$ samples and $\Delta t = T/4$, where $T = 1/f$ is the period of the signal. For a noise-free signal, these intensities would be given by

$$I_k = I_{\text{avg}}\left[1 + C\cos\left(\varphi + k\frac{\pi}{2}\right)\right], \quad (5)$$

where I_{avg} is the average of the sampled intensities.

The phase at the pixel γ, φ_γ, can be calculated from these intensity samples $[I_0^{(\gamma)} \ldots I_3^{(\gamma)}]$ with the four-point algorithm as

$$\varphi_\gamma = \arctan\left[\frac{I_3^{(\gamma)} - I_1^{(\gamma)}}{I_0^{(\gamma)} - I_2^{(\gamma)}}\right]. \quad (6)$$

Several other useful quantities can also be obtained from these four data points. Using the abbreviations

$$a_\gamma = I_0^{(\gamma)} - I_2^{(\gamma)}, \quad (7)$$

$$b_\gamma = I_3^{(\gamma)} - I_1^{(\gamma)}, \quad (8)$$

$$d_\gamma = I_0^{(\gamma)} + I_1^{(\gamma)} + I_2^{(\gamma)} + I_3^{(\gamma)}, \quad (9)$$

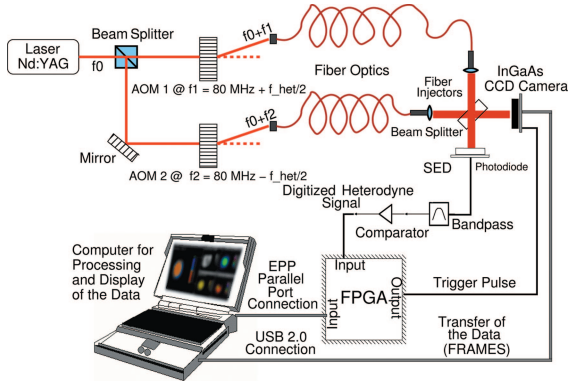

Fig. 1. (Color online) Experimental setup used for the phasemeter.

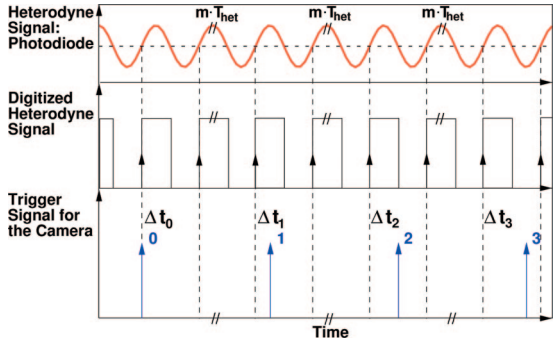

Fig. 2. (Color online) Time diagram of the signals processed to trigger the CCD camera. Note that the sinusoid is measured by the SED and yields a 180° phase shift with respect to the interference pattern measured by the CCD camera.

we get the following:

- Contrast at the pixel γ:

$$C_\gamma = 2\,\frac{\sqrt{a_\gamma{}^2 + b_\gamma{}^2}}{d_\gamma}. \tag{10}$$

- Total phase over the CCD surface:

$$\varphi_{\text{total}} = \arctan\left(\frac{\sum_\gamma b_\gamma}{\sum_\gamma a_\gamma}\right). \tag{11}$$

- Total contrast over the CCD surface:

$$C_{\text{total}} = 2\frac{\sqrt{\left(\sum_\gamma a_\gamma\right)^2 + \left(\sum_\gamma b_\gamma\right)^2}}{\sum_\gamma d_\gamma}. \tag{12}$$

- Average intensity at the pixel γ:

$$I_{\text{avg}}{}^{(\gamma)} = \frac{d_\gamma}{4}. \tag{13}$$

- The maximum and minimum intensity for the set of exposures ($I_0 \ldots I_3$) can also be determined for diagnostic purposes.

Furthermore, an exposure of the dark fringe can be directly captured by triggering the CCD camera with the appropriate delay τ_{df}:

$$\tau_{\text{df}} = \frac{3\pi/2 - \varphi_{\text{total}}}{2\pi}\,T_{\text{het}}. \tag{14}$$

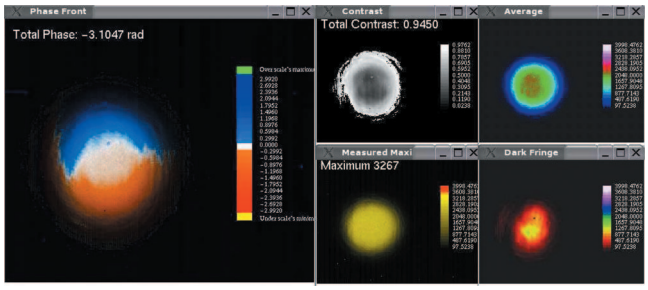

Fig. 3. (Color online) GUI programmed to display the measured data in real time.

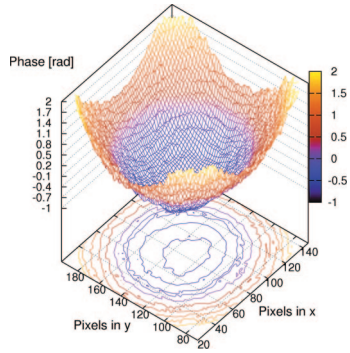

Fig. 4. (Color online) Spatial distribution of the phase.

3. Instrument Components and Setup

The interferometer configuration used in this experiment is a nonpolarizing heterodyne Mach–Zehnder interferometer. The light source was a Nd:YAG nonplanar ring oscillator laser with a wavelength of 1064 nm. Two acousto-optic modulators (AOMs), driven by slightly frequency shifted rf signals near 80 MHz, are used to generate two laser beams with a frequency difference of $f_{\text{het}} \approx 1623$ Hz. Since the beams diffracted by an AOM have a distorted non-Gaussian beam profile, single-mode polarization-maintaining fiber optics are used as mode cleaners. The requirements on the CCD camera are as follows:

- Every pixel must have simultaneous exposure (global shutter).
- The exposure time must be very short compared with the heterodyne period, $T_{\text{het}} \approx 1/1623$ Hz $= 616$ μs.
- The camera must be able to be triggered externally to allow frames to be captured at the required instances of time.
- The signal for each pixel needs to be proportional to the intensity on that pixel. Saturation effects, such as blooming, must be avoided.

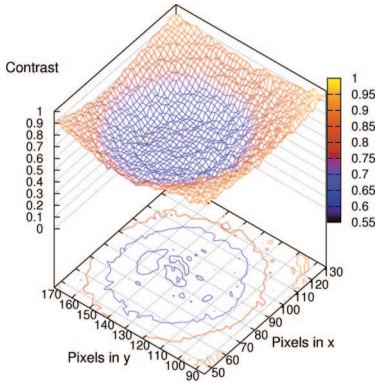

Fig. 5. (Color online) Spatial distribution of the contrast.

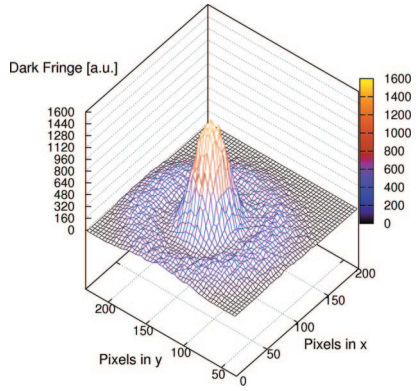

Fig. 6. (Color online) Exposure of a dark fringe.

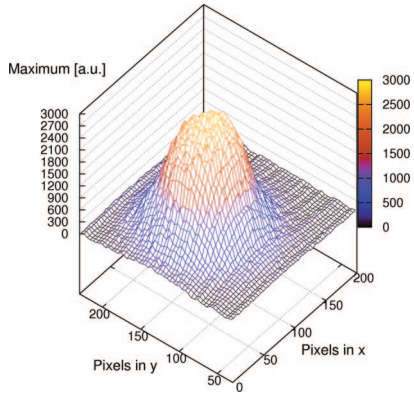

Fig. 8. (Color online) Maximum intensity over four exposures.

The CCD camera used is a model XEVA-USB from XenICs [17] with a 12-bit dynamic range that reaches 30 frames per second (fps) at a resolution of 320 $\times$ 256 pixels with a pixel pitch of 30 μm. The photosensitive chip is made of InGaAs, which has a quantum efficiency of approximately 80% for the near infrared (0.9–1.7 μm). The exposure time used was 1 μs (1/616 T_{het}). Ideally, the interference pattern should be sampled four times within a single heterodyne period of T_{het}. This would require a sampling period of $\Delta t = 154$ μs (approximately 6500 fps) for the CCD camera, which cannot be reached in practice because of the time required to transfer the image. To capture the intensity sample I_k, an integer number m of heterodyne periods T_{het} is added to Δt, and the trigger signal is sent to the CCD camera with the delay

$$\Delta t_k = mT_{\mathrm{het}} + \tau_k, \tag{15}$$

with $\tau_k = kT_{\mathrm{het}}/4$. The heterodyne period T_{het} is estimated by the timing control electronics of a field-programmable gate array (FPGA) at the beginning of the measurement as an average over 2000 periods and is then transfered to the PC through the parallel port interface. The experimental setup is outlined in Fig. 1. In practice, the environment is not stable enough to preserve a constant phase relationship over many periods of f_{het}. Hence, additional circuitry is used to resynchronize the trigger timing electronics with the actual phase of the heterodyne signal: A single-element photodiode (SED) is located at the second output of the interference beam splitter where the same interference pattern emerges with a 180° phase shift. The heterodyne signal measured by the SED is bandpass filtered and digitized by a comparator. When the phasemeter software is ready to capture the frame k, a command is sent from the PC to the FPGA through the parallel port, which includes the corresponding delay τ_k. The FPGA detects the rising edge of the digital heterodyne signal and triggers the camera with the controlled delay τ_k (see Fig. 2). The CCD camera captures the frame and transfers it to the PC through its USB 2.0 interface. After all four frames have been acquired, the phasemeter software computes the physical quantities described in Eq. (6)–(13) and an additional exposure is captured by triggering the camera with a delay τ_{df} given by Eq. (14), which corresponds to an exposure of the dark fringe.

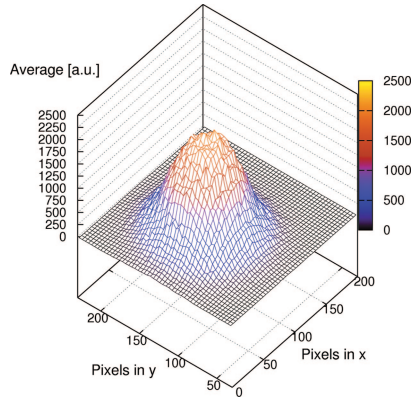

Fig. 7. (Color online) Average intensity over four exposures.

4. Results

A. Real-Time Operation

A graphical user interface (GUI) was developed to display the measured data in real time (see Fig. 3). The phasemeter reaches a rate of approximately 5–6 data displays per second and hence enables real-time mode matching of the beams, as well as an online optical alignment of an interferometer and optimal adjustment of its components. The five different displays in Fig. 3 are shown separately as three-dimensional representations in Fig. 4–8. These measurements were

Table 1. Main Noise Sources of the Phase Measurement

Noise Source	rms Phase Error
Laser power fluctuations	1.22 mrad
ADC digital noise of the camera	1.38 mrad
Time jitter	0.99 mrad
Total contribution	2.09 mrad
Noise level measured	2.96 mrad

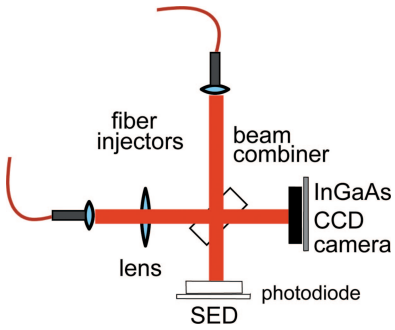

Fig. 9. (Color online) Experimental setup with an additional lens in the path of one beam to intentionally change the curvature of its wavefront.

conducted on a table-top Mach–Zehnder interferometer, as shown in Fig. 1.

B. Performance of the Phasemeter

To measure the noise level of the instrument, the camera was illuminated with a spatially homogeneous light source (an array of infrared LEDs behind a matte glass window), the intensity of which was modulated sinusoidally at a frequency of approximately 1623 Hz. This is a very stable test subject, ideal to determine the phase noise level of the instrument. It is expected that a flat phase front of the amplitude modulation can be obtained from this measurement since all pixels capture a similar sinusoidally modulated intensity with the same phase relationship. A series of real-time phase-front measurements were conducted in this configuration, determining the rms phase value at every pixel. Thus, a spatial rms phase variation of 2.96 mrad was measured over the CCD area of observation. According to Eq. (4), this value corresponds to a rms spatial resolution ΔL of approximately 500 pm.

As can be seen in Eq. (6), one noise source of the phase measurement is the fluctuation of the sampled intensities. The rms error of the phase, $\Delta\varphi_{\mathrm{rms}}$, induced by intensity fluctuations ΔI_{rms} can be estimated from Eq. (6) as

$$\Delta\varphi_{\mathrm{rms}} = \sqrt{\sum_k \left(\frac{\partial\varphi}{\partial I_k}\right)^2}\,\Delta I_{\mathrm{rms}} = \sqrt{\frac{2}{(I_0 - I_2)^2 + (I_1 - I_3)^2}}\,\Delta I_{\mathrm{rms}}. \tag{16}$$

After simplifying Eq. (16) by using Eq. (5), we obtain

$$\Delta\varphi_{\mathrm{rms}} = \frac{\sqrt{2}}{C}\,\frac{\Delta I_{\mathrm{rms}}}{I_{\mathrm{avg}}}. \tag{17}$$

The following three error sources were identified, and their noise contribution to the phase measurement was estimated:

1. Laser power fluctuations—An Allan deviation of 8.6×10^{-4} was measured at an averaging time of 33 ms, which corresponds to the sampling period of the CCD camera (30 fps), yielding a phase error of 1.22 mrad from Eq. (17).
2. Analog-to-digital converter digital noise of the camera—A rms intensity error of four quantization units was measured by constant and spatially homogeneous illumination of the CCD camera. The pixel-

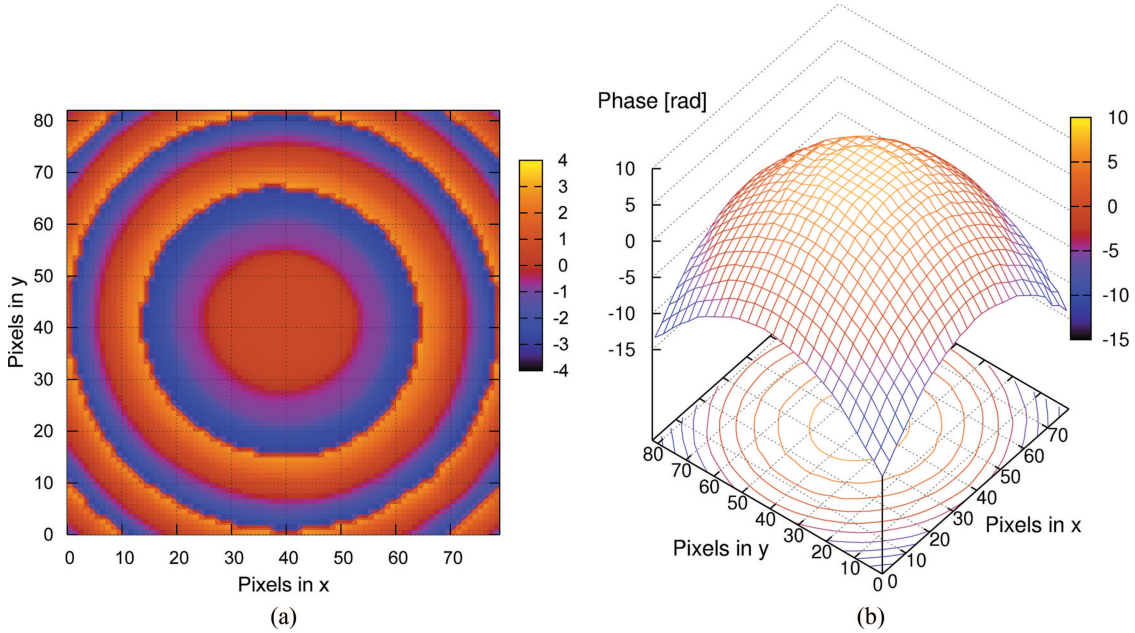

(a) (b)

Fig. 10. (Color online) (a) Phase front measured with a lens $f = +500$ mm in one arm of the interferometer. The phase front is clearly wrapped, due to the high curvature of the wavefront being transmitted through the lens with respect to the other one. (b) Phase front obtained by postprocessing the data measured in (a) with a two-dimensional phase-unwrapping algorithm.

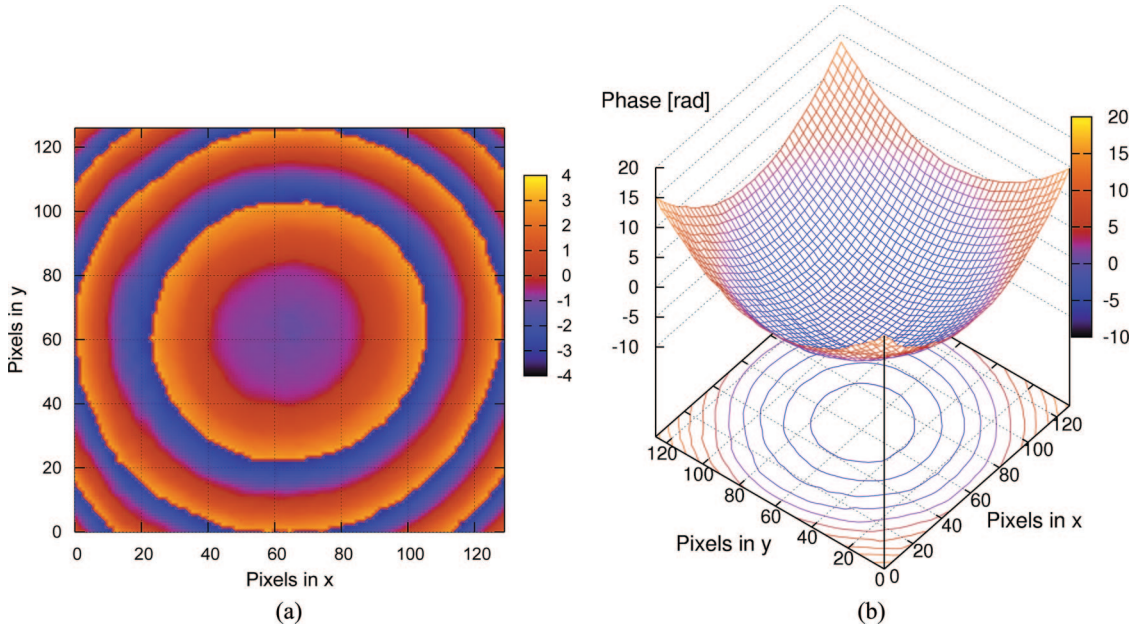

Fig. 11. (Color online) (a) Phase front measured with a lens $f = -500$ mm in one arm of the interferometer. (b) Phase front obtained from postprocessing the data of (a) with a two-dimensional phase-unwrapping algorithm.

wise rms variation and an average over the CCD surface were then computed. This value corresponds to a relative intensity fluctuation of 9.76×10^{-4}, which translates [by using Eq. (17)] into a phase error of 1.38 mrad.

3. Time jitter—There are at least three sources of jitter: first, the synchronization delay of the comparator output with respect to the 10 MHz clock of the FPGA, which is uniformly distributed between 0 and 100 ns; second, a similar delay between the FPGA clock and the CCD internal clock, which is also at 10 MHz but unsynchronized; and third, other jitter effects, such as apparent period fluctuations of the signal, due to setup conditional and limited stability, and the nonsynchronization between the FPGA and CCD clocks with the clock of the modulation electronics controlling the AOM's driving signal and therefore the heterodyne frequency generation. This latter effect is reduced (but not totally canceled) by retracking the timing control electronics to the rising edge of the digital heterodyne signal for each exposure. A phase error of 0.99 mrad was obtained by simulating the

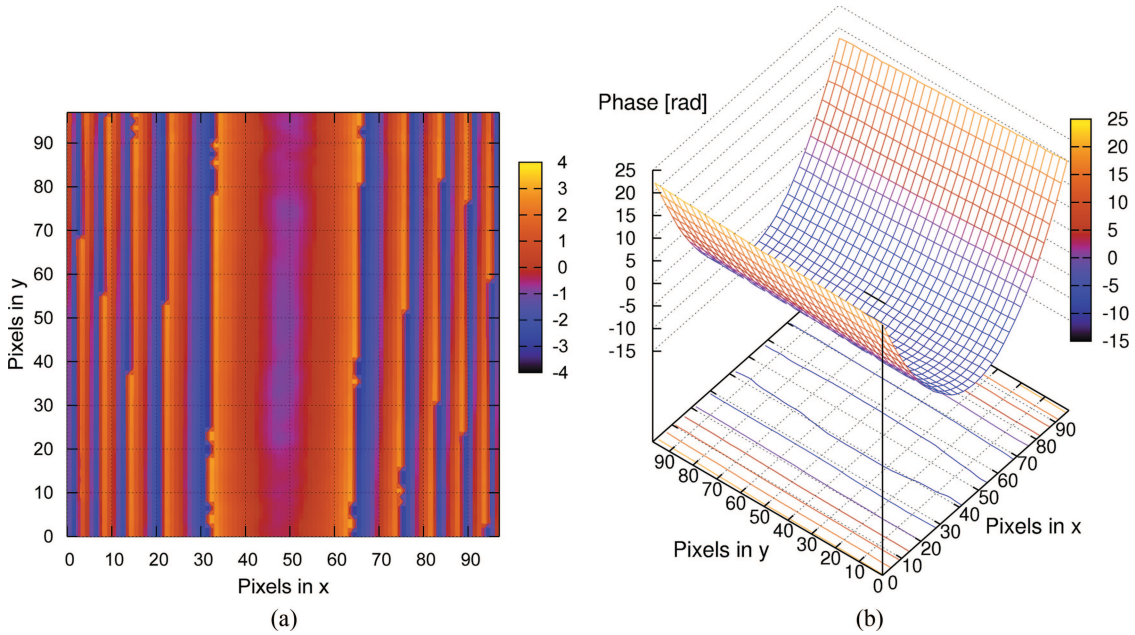

Fig. 12. (Color online) (a) Phase front measured with a cylindrical lens $f = +80$ mm in one arm of the interferometer. (b) Phase front obtained from postprocessing the data of (a) with a two-dimensional phase-unwrapping algorithm.

first and second effects in software, using two independent random delays uniformly distributed.

Table 1 summarizes the noise contributions identified for the phase measurement.

C. Measurements

To test the functionality of the phasemeter, a series of measurements were conducted on the table-top interferometer shown in Fig. 1. The aim of these measurements was to intentionally change the curvature of one of the interfering wavefronts and to use the phasemeter to read out the spatial distribution of the phase. Since the two interfering wavefronts are similar, a lens was introduced into the path of one beam, between the corresponding fiber injector and the beam combiner (see Fig. 9). The results of these measurements are shown in Figs. 10–12. Three different type of lenses were used: $f = +500$ mm (Fig. 10), $f = -500$ mm (Fig. 11), and a cylindrical lens with $f = +80$ mm (Fig. 12). The curvature of the wavefront considerably increases (due to the lens) such that it covered several wavelengths in the area of observation. The resulting phase front measured is wrapped as can be recognized by the phase rings in Fig. 10(a) and 11(a) and the stripes in Fig. 12(a). A two-dimensional phase-unwrapping algorithm [18–20] was developed and was used for postprocessing these data. The result of this postprocessing is shown in Figs. 10(b), 11(b), and 12(b). It can be seen, by comparing Figs. 10(b) and 11(b), that the inflection of the phase-front curvature changes according to the focal length of the lens used (±500 mm). Within the LTP interferometry research and development, this instrument will be used during manufacture of the optical bench interferometer flight model. The lenses of the fiber injectors can be adjusted such that the difference in curvature between the two interfering wavefronts are minimized by using the real-time phase-front readout provided by this phasemeter. A phase-front measurement was already conducted at the optical bench engineering model for LTP [11,21]. These results are presented in Fig. 13 and clearly show an inhomogeneous phase front, which can be attributed to nonoptimal adjustment of the lenses in the two fiber injectors. A further test was done on a table-top interferometer to adjust the lenses of two commercial fiber injectors by using this instrument. The aim of this adjustment was to match the parameters of the interfering beams and to obtain a homogeneous flat phase front. The result of this experiment is shown in Fig. 14. A considerable improvement was achieved in matching the shape of the two beams (compare the phase scale of the plots in Figs. 13 and 14). It can be seen that over a surface of approximately 1.2 mm × 1.2 mm the phase front shows a considerably homogeneous spatial profile. We analyzed a circular section of approximately 1 mm diameter at the beam center. The standard deviation of these data is 3.49 mrad, which is very close to the measured sensitivity of the instrument. This value corresponds to a spatial resolution of 590 pm and amounts to a considerable improvement in the correction of the beam shapes.

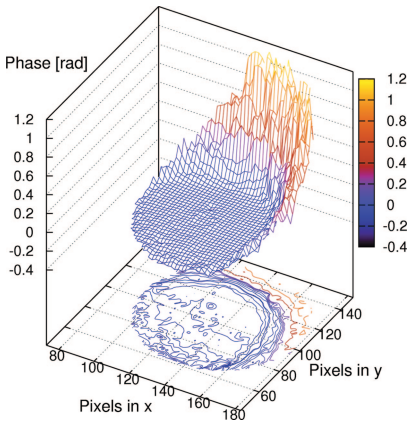

Fig. 13. (Color online) Phase front measured at the engineering model of the optical bench for the LTP.

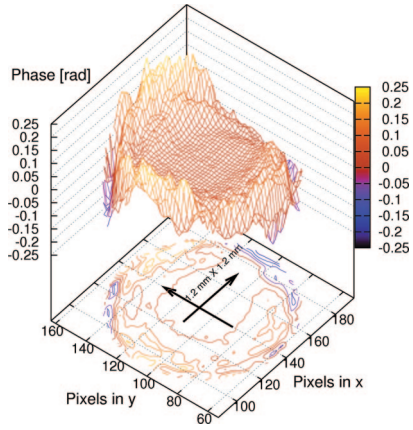

Fig. 14. (Color online) Adjusted phasefront measured on a table-top Mach–Zehnder interferometer.

5. Conclusions

We have developed an instrument that allows real-time phase-front detection and mode-mismatch characterization of two interfering beams in a heterodyne interferometer. A rms noise level of 2.96 mrad, which corresponds to a wavefront roughness of 500 pm, was obtained experimentally. This makes it possible to optimize the beam shapes by adjusting the optical components in real time with the help of the data displayed onto the GUI (5–6 data displays per second). The results shown in Figs. 10–12 demonstrate the proper functionality of the instrument. By using well-matched wavefronts, this method can also be used to analyze, and measure accurately, surfaces and optical components down to subnanometer levels. It is planned that this instrument be used in the manufacturing of the flight model of the optical bench for the LISA Technology Package.

The authors kindly thank Albrecht Rüdiger, Benjamin Sheard, Paul Cochrane, Alexander Bunkowski, James DiGuglielmo, and Martin Hewitson for their

valuable contributions in reviewing and improving various parts of the manuscript.

References

1. A. E. Siegman, *Lasers* (University Science Books, 1986).
2. HASO II User Manual, Imagine Optic, Rue Charles de Gaulle 18, F-91400 Orsay, France.
3. G. Lai and T. Yatagai, "Generalized phase-shifting interferometry," J. Opt. Soc. Am. A **8,** 822–826 (1991).
4. J. Millerd, N. Brock, J. Hayes, B. Kimbrough, M. Novak, M. North-Morris, and J. C. Wyant, "Modern approaches in phase measuring metrology," Proc. SPIE **5856,** 14–22 (2005).
5. S. Kaiser, T. Maier, A. Grossmann, and C. Zimmermann, "Fizeau interferometer for phase-shift interferometry in ultrahigh vacuum," Rev. Sci. Instrum. **72,** 3726–3727 (2001).
6. Y. Surrel, "Fringe analysis," Top. Appl. Phys. **77,** 55–102 (2000).
7. K. Hibino, B. F. Oreb, D. I. Farrant, and K. G. Larkin, "Phase-shifting algorithms for nonlinear and spatially nonuniform phase shifts," J. Opt. Soc. Am. A **14,** 918–930 (1997).
8. Y. Li, Z. Zhu, and X. Li, "Elimination of reference phase errors in phase-shifting interferometry," Meas. Sci. Technol. **16,** 1335–1340 (2005).
9. R. Shagam and J. C. Wyant, "Optical frequency shifter for heterodyne interferometers using multiple rotating polarization retarders," Appl. Opt. **17,** 3034–3035 (1978).
10. F. Zhao, "Picometer laser metrology for the Space Interferometry Mission (SIM)," in *Conference on Lasers and Electro-Optics (CLEO),* Vol. 96 of Trends in Optics and Photonics Series (Optical Society of America, 2004), paper CTuo5.
11. G. Heinzel, C. Braxmaier, R. Schilling, A. Rüdiger, D. Robertson, M. te Plate, V. Wand, K. Arai, U. Johann, and K. Danzmann, "Interferometry for the LISA technology package (LTP) aboard SMART-2," Class. Quantum Grav. **20,** 153–161 (2003).
12. H. Zhao and G. Zhang, "Nonlinear error by orientation and elliptic polarization in a two-beam interferometer," Opt. Eng. **41,** 3204–3208 (2002).
13. V. Wand, J. Bogenstahl, O. Braxmaier, K. Danzmann, A. García, F. Guzmán, G. Heinzel, J. Hough, O. Jennrich, C. Killow, D. Robertson, Z. Sodnik, F. Steier, and H. Ward, "Noise sources in the LTP heterodyne interferometer," Class. Quantum Grav. **23,** 159–167 (2006).
14. G. Heinzel, V. Wand, A. Garcia, O. Jennrich, C. Braxmaier, D. Robertson, K. Middleton, D. Hoyland, A. Rüdiger, R. Schilling, U. Johann, and K. Danzmann, "The LTP interferometer and phasemeter," Class. Quantum Grav. **21,** 581–587 (2004).
15. D. Robertson, C. Killow, H. Ward, J. Hough, G. Heinzel, A. García, V. Wand, U. Johann, and C. Braxmaier, "LTP interferometer-noise sources and performance," Class. Quantum Grav. **22,** 155–163 (2005).
16. K. Freischlad and C. L. Koliopoulos, "Fourier description of digital phase-measuring interferometry," J. Opt. Soc. Am. A **7,** 542–551 (1990).
17. XFPA-320*256 User Manual, XenICs n.v., Kapeldreef 75, B-3001 Leuven, Belgium, July 2003.
18. D. C. Ghiglia and L. A. Romero, "Robust two-dimensional weighted and unweighted phase unwrapping that uses fast transforms and iterative methods," J. Opt. Soc. Am. A **11,** 107–117 (1994).
19. T. J. Flynn, "Two-dimensional phase unwrapping with minimum weighted discontinuity," J. Opt. Soc. Am. A **14,** 2692–2701 (1997).
20. D. C. Ghiglia and M. D. Pritt, *Two-Dimensional Phase Unwrapping: Theory, Algorithms, and Software* (Wiley, 1998).
21. G. Heinzel, C. Braxmaier, M. Caldwell, K. Danzmann, F. Draaisma, A. García, J. Hough, O. Jennrich, U. Johann, C. Killow, K. Middleton, M. te Plate, D. Robertson, A. Rüdiger, R. Schilling, F. Steier, V. Wand, and H. Ward, "Successful testing of the LISA Technology Package (LTP) interferometer engineering model," Class. Quantum Grav. **22,** 149–154 (2005).